RSC Advances

PAPER

Cite this: *RSC Adv.*, 2019, **9**, 27378

First principles study of g-Mg_3N_2 as an anode material for Na-, K-, Mg-, Ca- and Al-ion storage†

Lixin Xiong,[a] Hewen Wang,*[b] Wan Xiong,[a] Shicheng Yu[a] and Chuying Ouyang *[a]

Received 9th August 2019
Accepted 26th August 2019

DOI: 10.1039/c9ra06189d

rsc.li/rsc-advances

Searching for electrode materials for non-lithium metal ion batteries (NLMIBs) is key to the success of NLMIBs. In this work, we investigated the scientific feasibility of using g-Mg_3N_2, which is a novel 2D graphene-like material, as an anode for non-lithium metal-ions (Na, K, Mg, Ca and Al) batteries based on density functional theory calculations. The sequential adsorption energy, Bader charge, intercalation voltage, energy-storage capacity, electronic conductivity and metal-ion diffusion energy barrier are calculated. Results show that the metal-ion intercalation potentials and diffusion energy barriers are suitable for battery application. The maximum specific capacities for Na-, K-, Mg-, Ca- and Al-ion on g-Mg_3N_2 are predicted to be 797, 797, 531, 1594 and 797 mA h g^{-1}, respectively. The excellent structural stability of g-Mg_3N_2 is good for the cycling performance. Moreover, the electronic structure of the g-Mg_3N_2 changes from semiconductor to metal upon metal-ion adsorption, as well as relatively low metal-ion diffusion energy barriers (except for Al-ion diffusion), are beneficial to the charge/discharge rate of the g-Mg_3N_2 anode.

1. Introduction

Developing sustainable and renewable energy to replace traditional fossil fuels has always been a significant challenge in the world.[1,2] The rapid development and application of wind and solar energies has motivated researchers to look for novel energy storage materials with larger capacities and longer cycling life.[3] Lithium-ion batteries (LIBs) as outstanding energy storage systems have been hugely successful in portable electronic devices for decades.[4] The excellent performance of LIBs, such as high working voltage and energy density, good cyclic stability and environmental friendliness, is exactly what portable electronic devices and electric vehicles (EVs) need for power supply.[5,6] However, the inadequate natural abundance of lithium reserves, which in turn leads to expensive commercial cost, restricts the wide application of LIBs in large-scale electrical energy storage and EVs.[7] Therefore, new metal-ion batteries utilizing other elements such as Na,[8] K,[9] Mg,[10] Ca[11] and Al[12] have been considered as potential alternatives to LIBs. These substitutes should possess low redox potentials, high specific capacities, excellent cyclic stability and most importantly, low cost.[13]

The key to the success of non-lithium metal-ion batteries (NLMIBs), which use non-lithium metal-ions as charge carrier, is the properties of corresponding electrolyte and electrode materials.[14,15] Therefore, searching for new electrode materials with appropriate performance becomes urgent from the scientific point of view. Recently, many cathode materials for NLMIBs have been reported such as framework materials,[16,17] polyanion compounds[18,19] and layered transition-metal oxides.[20,21] However, due to the larger ionic radius and higher valence state of non-Li metal-ions, the use of conventional LIBs anode materials in NLMIBs is unsatisfactory.[22,23] Fortunately, 2D materials were found to have potential applications as anodes for NLMIBs, both experimental and theoretically.[24,25] For example, MXenes are considered as promising anode materials for NLMIBs due to their unique 2D structural character, which benefits fast metal-ion diffusion and provides more space for metal-ion storage.[26–28] Mortazavi *et al.* found that the flat borophene is promising anode material with superhigh capacities of Na- (1640 mA h g^{-1}) and Mg-ion (2480 mA h g^{-1}) storage.[29] They also revealed the outstanding performance of boron-graphdiyne as an anode material with ultrahigh capacities of 808 and 5174 mA h g^{-1} for Na- and Ca-ion storage.[30] Lei *et al.* predicted that B_2S monolayer is a promising anode material for Na- and K-ion batteries with high energy density and low diffusion barriers.[31] Demiroglu *et al.* reported that the MXene electrode materials of Ti_2CO_2 and V_2CO_2 are promising for Na-ion battery applications, Ti_2CO_2 could be applied as low voltage applications and V_2CO_2 is more appropriate for higher voltages.[32]

Recently, a novel 2D material g-Mg_3N_2 was predicted to be a stable graphene-like structure by a global particle-swarm optimization method.[33] It was found that the cohesive energy difference between the monolayer g-Mg_3N_2 and bulk phase

[a]*Department of Physics, Laboratory of Computational Materials Physics, Jiangxi Normal University, Nanchang, 330022, China. E-mail: cyouyang@jxnu.edu.cn*

[b]*College of Chemistry and Chemical Engineering, Hubei Key Laboratory for Processing and Application of Catalytic Materials, Huanggang Normal University, Huanggang, 438000, P. R. China. E-mail: wanghewen2014@126.com*

† Electronic supplementary information (ESI) available. See DOI: 10.1039/c9ra06189d

Mg_3N_2 is only 0.01 eV per atom, which leads to good chemical stability of the g-Mg_3N_2 that is capable of withstanding temperatures higher than 2000 K. The planar geometry of the g-Mg_3N_2 is highly graphene-like, and thus the advantages of graphene can also be found in the g-Mg_3N_2. In order to take the graphene-like advantages of g-Mg_3N_2, it is worthwhile to investigate the scientific possibility of applying g-Mg_3N_2 as an anode material for NLMIBs.

First-principles calculations are proved to be a reliable tool to study the metal-ion adsorption, electrochemical potential, electronic conductivity and ionic diffusion in electrode materials for NLMIBs.[34–36] In this paper, we systematically investigated Na-, K-, Mg-, Ca- and Al-ion storage behaviors in g-Mg_3N_2 with first-principles calculations. We begin our work from single metal-ion adsorption on g-Mg_3N_2 in three particular sites, followed by a performance evaluation of g-Mg_3N_2 as an anode material for NLMIBs. The intercalation potential, theoretical capacity, electronic structure, and metal-ion diffusion are studied. We finally conclude that g-Mg_3N_2 has potential application as an excellent anode material for NLMIBs.

2. Computational method

In this paper, all calculations are implemented by the Vienna Ab initio Simulation Package (VASP) based on density functional theory (DFT).[37] Projector augmented wave (PAW) method in combination with the generalized gradient approximation (GGA) expressed by the Perdew–Burke–Ernzerhof (PBE) functional are used.[38,39] The cutoff energy for the plane-wave is chosen to be 550 eV for all calculations. van der Waals corrections are included *via* using the DFT-D3 method to better describe the dispersion interactions between adsorbed metal-ions and host 2D materials.[40,41] The lattice parameters as well as the ionic positions are adequately optimized until the ultimate atomic forces and the internal stresses are converged to 0.02 eV $Å^{-1}$ and 0.1 kbar, respectively. The density of states (DOS) are calculated by the Gaussian smearing method with a smearing width of 0.05 eV. The monolayer 2D host material is separated by a 15 Å vacuum layer along the *z*-axis direction. The Monkhorst–Pack scheme 5×3 and 3×3 *k*-point mesh are used for orthogonal unit cell and the 2×1 supercell, respectively.[42] The nudged elastic band (NEB) method is applied to optimize the metal-ions migration paths and evaluate the energy barriers.[43] The charge distribution among metal-ions and 2D host is analyzed by the Bader charge analysis.[44] The phonon dispersion data are calculated using the linear response method, and the phonon data is collected with the PHONOPY code.[45]

Adsorption energies E_{ad} are used to measure the metal-ions adsorption strength on the 2D host material. Meanwhile, the amount of metal-ions storage on g-Mg_3N_2 can be evaluated by the sequential adsorption energies defined as:

$$E_{ad} = E_{host+(n+1)M} - E_{host+nM} - E_M \quad (1)$$

where E_M, $E_{host+(n+1)M}$, and $E_{host+nM}$ are the calculated ground state energies of the gas phase metal-atom in vacuum, and the g-Mg_3N_2 host with $(n + 1)$ and n metal-ions adsorbed, respectively. If the metal-ions adsorption energy is lower than the cohesive energy of the bulk phase metals, which are defined as the total energy difference of one metal-atom in its bulk phase metal and its gas phase state in vacuum, the intercalation potential is positive. As the intercalation potential is also dependent on the adsorption concentration, we need to calculate the sequential intercalation potential, which is defined as:

$$V = -\frac{E_{M_{x_2}Mg_3N_2} - E_{M_{x_1}Mg_3N_2} - (x_2 - x_1)E_M}{(x_2 - x_1)ne} \quad (x_2 > x_1) \quad (2)$$

where $E_{Mx_2Mg_3N_2}$, $E_{Mx_1Mg_3N_2}$, and E_M are the total energies (in eV) of the $M_{x_2}Mg_3N_2$, $M_{x_1}Mg_3N_2$ and one metal atom in its bulk phase metals, respectively. $x_2 - x_1$ is the number of metal-ions intercalated/deintercalated, and n refers to the corresponding valence electrons of the metal-ion.[46,47] The maximum theoretical capacity (C_M) can be estimated by the following equation:

$$C_M = \frac{x_{max} nF}{M_{Mg_3N_2}} \quad (3)$$

where x_{max}, n, F and $M_{Mg_3N_2}$ are the maximum number of adsorbed metal-ions, the number of corresponding metal-ion's valence electrons, the Faraday constant and the mass of $M_{Mg_3N_2}$, respectively. The x_{max} is maximum number of metal-ions that can be adsorbed on the g-Mg_3N_2 before the potential decreased to 0 V.

3. Results and discussions

3.1 Single metal-ion adsorption on g-Mg_3N_2

The space group of g-Mg_3N_2 is *P*6/*mmm* (no. 191), with N atoms occupying 3g Wyckoff position and Mg atoms occupying another 3g Wyckoff position, as shown in Fig. 1(a). The optimized lattice constants of primitive unit cell are $a = b = 6.6316$ Å, in good agreement with previous reports.[33,48] In order to better demonstrate of the metal-ions adsorption sites, we use the orthogonal unitcell that includes 6 Mg and 4 N atoms, as shown in Fig. 1(b). According to the symmetry of the g-Mg_3N_2 in the orthogonal unitcell, only three sites are considered for metal-ions adsorptions. B-site is the bridge sites of N atoms (also top of the Mg atom), H-site is the center of hexagon ring and T-site is top of the N atom. Fig. 1(c–g) show the relaxed atomic structures with corresponding metal-ions adsorbed on each site.

Table 1 presents the detailed information on energetics, structural and charge transfer of the g-Mg_3N_2 after single metal-ion adsorption. After any metal-ion adsorption on B-sites (top of Mg atom), the corresponding Mg atom moved downwards and out of the graphene-like plane due to the repulsive interaction between them. As for different metal-ions adsorbed on the T-site, the negatively charged N atom and positively charged metal-ions attract each other and the N atom moves toward the metal-ions. Adsorption energies of different metal-ions in H-site are higher than corresponding bulk phase metal cohesive energies, which are calculated to be −1.248, −0.999, −1.734, −2.066 and −3.678 eV for Na, K, Mg, Ca and Al, respectively. This shows that H-site is not suitable for metal-ion adsorption

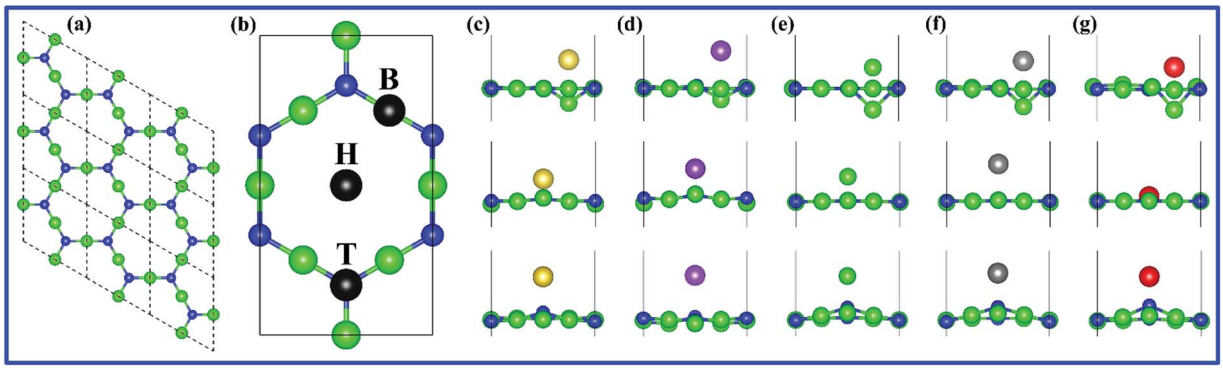

Fig. 1 The top views of the atomic structure of the hexagonal g-Mg_3N_2 primitive cell (a) and the orthogonal g-Mg_6N_4 unitcell with metal-ions (black spheres) adsorption at B (bridge), T (top), and H (hollow) sites (b). (c)–(g) are the side views of the atomic structures with single metal-ion adsorption at B (up), H (middle), and T (down) sites after relaxation. The green, blue, yellow, purple, gray and red spheres denote Mg, N, Na, K, Ca and Al atoms, respectively.

from energetics point of view, and thus H-site is no longer considered in later calculations. Meanwhile, the adsorption energies of different metal-ions in both B-site and T-site are thermodynamics favorable. The Bader charge analysis suggests that the adsorption energies are strongly correlated with the charge loss of the metal-ions, namely, the more electrons metal-ions lose, the lower system energy is. This indicates the Coulomb interaction dominates the energetics of the metal-ion adsorption on g-Mg_3N_2. As Mg atom and metal-ions are positively charged while N is negatively charged, metal-ions at T-site have the strongest attractive force from the closest N-atom (please refer to the distances of metal to Mg atoms d_{M-Mg} and N atoms d_{M-N} given in Table 1). However, due to the repulsive forces from three nearest neighboring Mg atoms, adsorption energies at T-sites are higher than the corresponding metal-ion adsorption at B-sites. When metal-ions adsorbed at the B-site, there are two nearest neighboring N atoms attracting to them, as shown in Fig. 1(b). As for H-site, the N-distance is larger than the Mg-distance, leading to the stronger repulsive interaction and the weaker attractive interaction. Consequently, all metal-ions adsorption energies at H-sites are high and not suitable for metal-ion storage.

3.2 Theoretical specific capacity and intercalation potential

Due to the repulsive interactions among positively charged metal-ions, the adsorption energies are also sensitive to the metal-ion adsorption concentration and increases with the increased concentration. Meanwhile, in order to figure out the maximum amounts of metal-ions that can be adsorbed on the g-Mg_3N_2 surface before the adsorption energies reach the cohesive energy of the corresponding bulk phase metals, we calculated the sequential adsorption energies at different metal-ions concentrations. We gradually add metal-ions according to above single atom adsorption sites and energies until the sequential adsorption energies become close to the cohesive energies of the corresponding bulk phase metal. At the same concentration of metal-ions, we choose the adsorption configuration with the lowest energy. The adsorption energies as a function of the metal-ion adsorption concentration are presented in the ESI (Fig. S1†), from which we can see that the maximum numbers of Na-, K-, Mg-, Ca- and Al-ions can be adsorbed on the unitcell of the g-Mg_6N_4 are 6, 6, 2, 6 and 2, respectively. The atomic structures and arrangement of the adsorbed metal-ions are presented in Fig. 2(a–e). The corresponding theoretical capacities for Na^+, K^+, Mg^{2+}, Ca^{2+} and Al^{3+} are 797, 797, 531, 1594 and 797 mA h g^{-1}, respectively.

In addition to the theoretical capacity, voltage is another important character of an electrode material. Since lower anode potential is beneficial for higher output voltage of the battery system, relatively low intercalation potential of an anode material is expected. The intercalation potentials on g-Mg_3N_2 as a function of their theoretical capacities are presented in Fig. 2(f). As is shown, the obtained potentials are acceptable for

Table 1 The transferred charges (Δq) from metal-ions by Bader, the adsorption energies (E_{ad}), the vertical distance from the metal-ion to the 2D host plane (height) and the distance from metal-ion to its nearest neighboring N/Mg atoms (Mg-, N-distance)

	Δq (e)			E_{ad} (eV)			Height (Å)			d_{M-Mg} (Å)			d_{M-N} (Å)		
	B	H	T	B	H	T	B	H	T	B	H	T	B	H	T
Na	−0.749	−0.601	−0.673	−1.728	−1.143	−1.385	1.889	1.385	2.669	2.711	3.632	3.340	2.423	4.048	2.276
K	−0.753	−0.720	−0.704	−1.687	−1.333	−1.426	2.432	1.897	2.907	3.088	3.922	3.628	2.830	4.222	2.656
Mg	−1.107	−0.017	−0.812	−2.060	−0.898	−1.321	1.448	1.572	2.596	2.624	3.655	3.137	2.043	4.139	2.021
Ca	−1.186	−0.571	−0.803	−3.082	−1.143	−2.117	1.836	2.382	2.789	2.864	4.081	3.293	2.260	4.499	2.168
Al	−1.404	+0.289	−0.782	−3.716	−1.526	−2.901	1.414	0.300	2.625	2.642	3.287	3.198	1.892	3.843	1.844

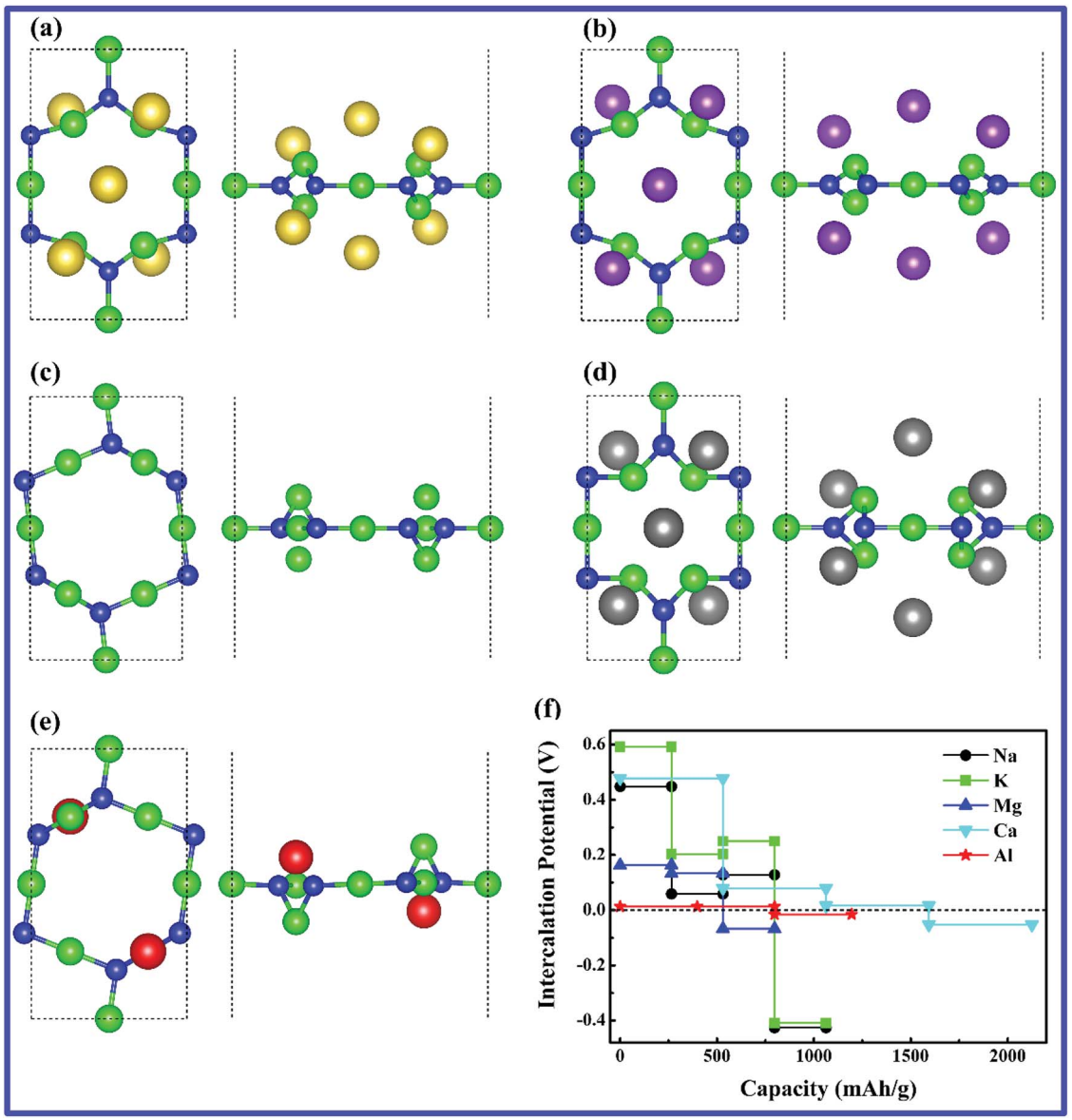

Fig. 2 Metal-ions adsorption configurations of maximum theoretical capacity are shown in (a)–(e), the green, blue, yellow, purple, gray and red spheres denote Mg, N, Na, K, Ca and Al atoms, respectively. The calculated sequential metal-ions intercalation potentials on g-Mg_3N_2 as a function of theoretical capacity are showed in (f).

NLMIBs anode applications. The theoretical capacity and voltage are negatively correlated, which can be attributed to the weakened attractive electrostatic interaction between the metal-ions and the 2D host and the enhanced repulsive electrostatic interactions among the metal-ions at a higher concentration.

As an anode material, the structural stability of the g-Mg_3N_2 is also very important, particularly after the metal-ion is adsorbed (discharged states). In order to test the structural and thermal stability of the g-Mg_3N_2 anodes, phonon dispersion curves calculated and AIMD simulations are performed. The phonon dispersion curves of pristine g-Mg_3N_2 as well as Na- and Mg-ion adsorbed cases ($Na_1Mg_3N_2$ and $Mg_1Mg_3N_2$) are presented in the ESI (Fig. S2†). As is seen, imaginary frequencies are not observed, showing that these structures are dynamically stable at their ground states. Furthermore, AIMD simulation results (refer to ESI Fig. S3† for details) also suggest that the thermal stability of the g-Mg_3N_2 can be stable at 300 K, even at the highest metal-ion adsorption concentrations ($Na_3Mg_3N_2$ and $Mg_1Mg_3N_2$). The phonon dispersion curves and the AIMD simulation results suggest that the g-Mg_3N_2 anode may have good cycling stability.

3.3 The charge/discharge rate performance of g-Mg_3N_2

The speed of charge/discharge is an important consideration in battery applications. The charge/discharge rate performance of an anode material is determined by the electronic conductivity and metal-ions diffusivity. Here we considered both of them to evaluate the rate performance of g-Mg_3N_2. The electronic

density of states (DOS) of the g-Mg_3N_2 before and after metal-ion adsorption are presented in Fig. 3. As is seen, the intrinsic electronic structure of the g-Mg_3N_2 is undesirable semiconductor (band gap 0.91 eV). However, upon different concentrations and species of metal-ions adsorption, the electronic structures become metallic, as is shown in Fig. 3(b–f). This is beneficial to improve the electronic conductivity during the charge/discharge process. In addition, we also found that except Al, the more metal-ions are adsorbed, the higher intensity of the DOS around the Fermi level is observed. Above results indicate that more active electrons are created in the system during metal-ions adsorption process, showing better electronic conductivity can be obtained at higher concentrations.

We had demonstrated that g-Mg_3N_2 have good electronic conductivity after metal-ions adsorbed, next we will probe the metal-ions diffusions on the g-Mg_3N_2. Previous reports had already shown that the 2D materials possess high diffusion coefficient and low migration energy barriers.[36,49,50] Since the metal-ions migration energy barrier is related to the metal-ion concentration, we construct a 2 × 1 orthogonal supercell to reduce the influence from periodic boundary conditions. As discussed above, all metal-ion prefers to stay at the most energetically stable adsorption B-site. Therefore, we only consider the different metal-ions migrations from one B-site to its neighboring B-site.

Fig. 4(e) shows all possible pathways for single metal-ion migration on the g-Mg_3N_2 surface. The name of pathway is ranked by the length, the shortest distance pathway is named Path-1, and the longest pathway is named Path-4. In fact, the Path-3 for Na-, K- and Ca-ion are finally become the same as Path-2 during the NEB calculation. For all positive charged metal-ions during migrations, the more positive charges they carried, the stronger repulsive force they experienced. Thus, the Na^+ and K^+ migration energy barriers are much lower compared

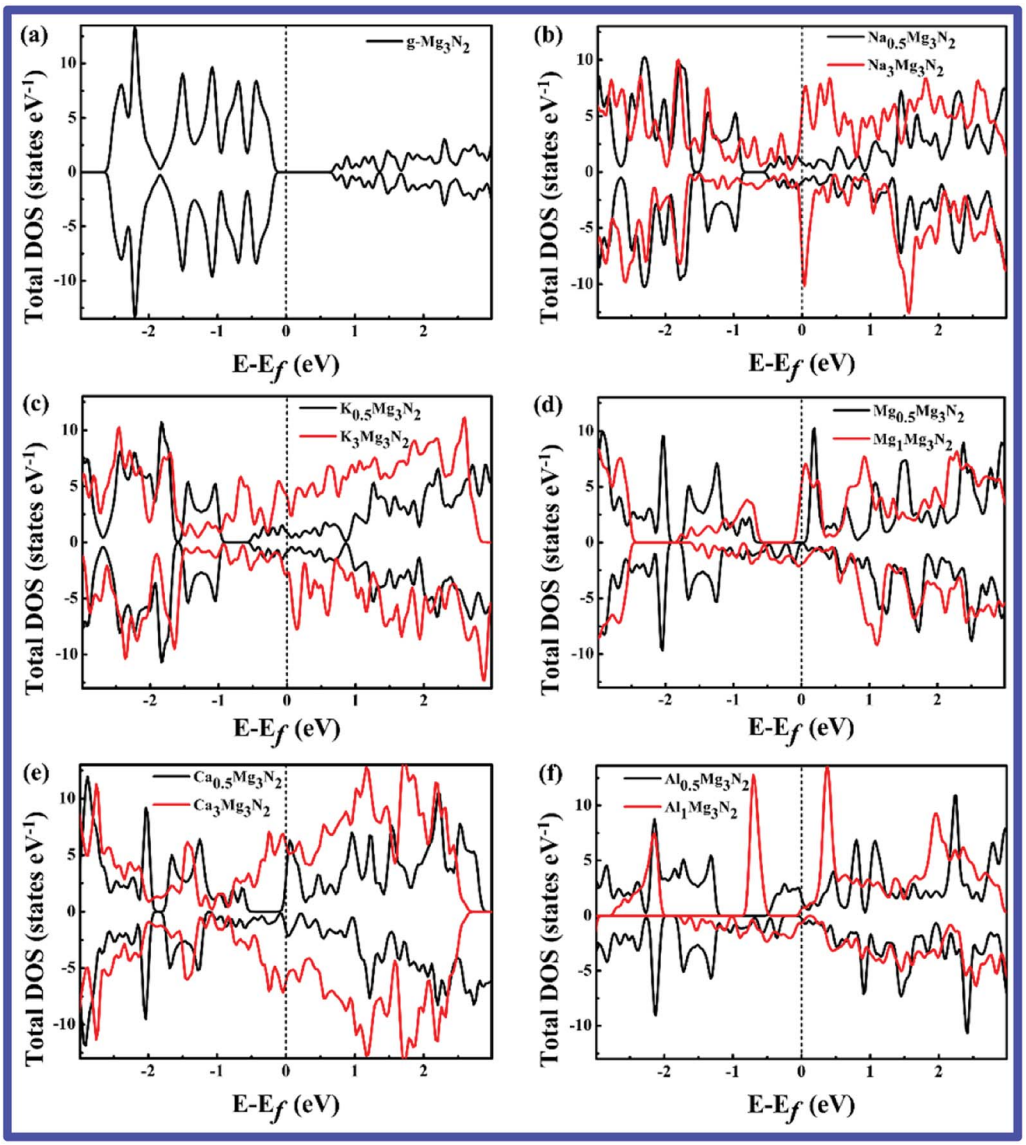

Fig. 3 The total DOS of the intrinsic g-Mg_3N_2 (a) and its corresponding M adsorbed states $M_xMg_3N_2$ (b)–(f) with $x = 0.5$ and 1 or 3.

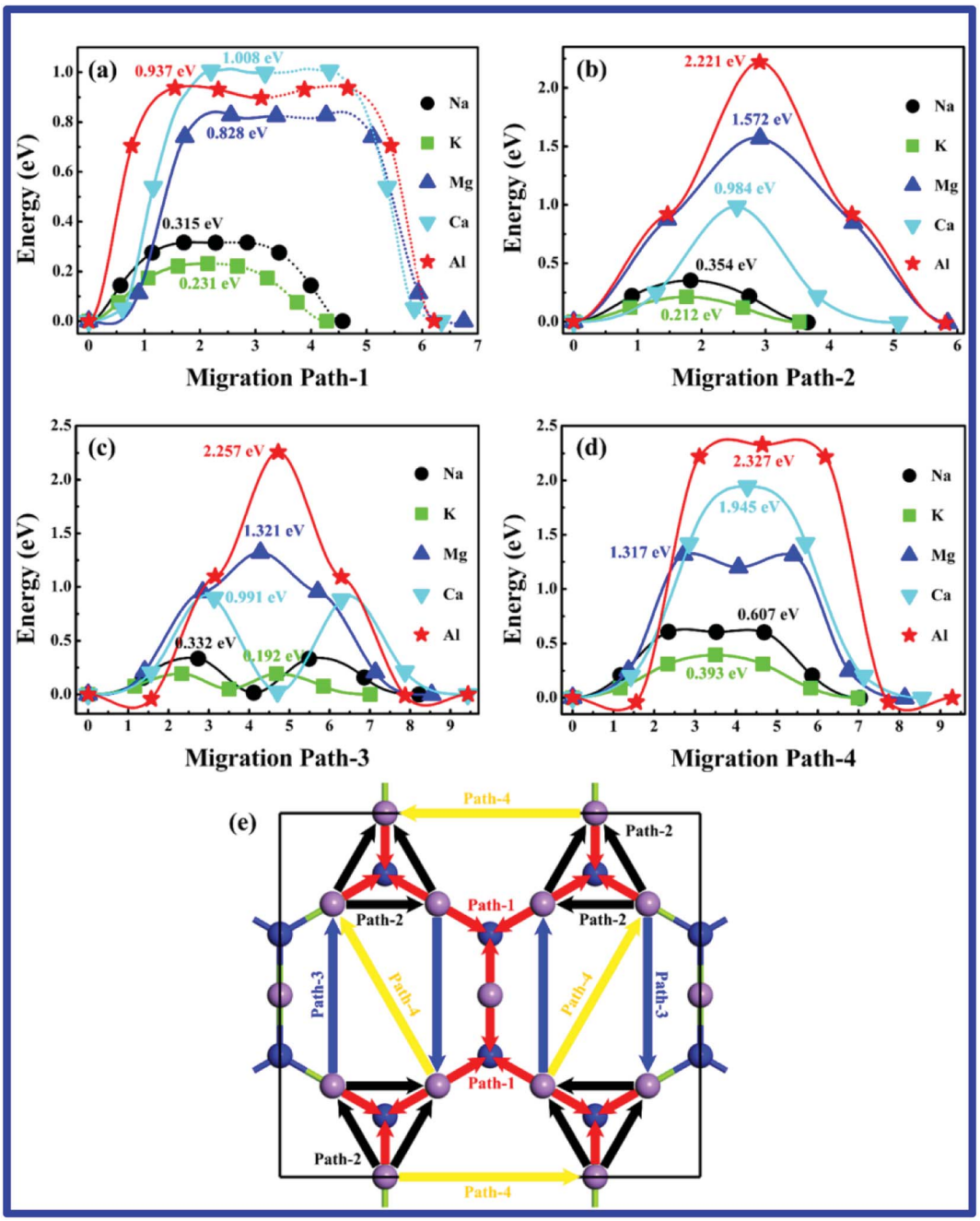

Fig. 4 The metal-ions migration pathways on g-Mg_3N_2 (e) and the energy profiles along the optimized pathways (a–d) on g-Mg_3N_2. The blue and purples spheres represent the N atoms and different metal-ions adsorbed upon the Mg atom (B-site). The 2D metal-ions diffusion networks are illustrated by four colored arrows.

with Mg^{2+}, Ca^{2+} and Al^{3+} during all migration pathways. The obtained the migration energy barriers of all metal-ions are shown in Fig. 4(a–d). The lowest migration energy barriers for Na^+, K^+, Mg^{2+}, Ca^{2+} and Al^{3+} are 315 meV in Path-1, 192 meV in Path-3 (actually Path-2), 828 meV in Path-1, 984 meV in Path-2 and 937 meV in Path-1, respectively. In general, large ion radius would restrict the capacity and rate performance. However, our results show the charge of metal-ions, rather than the ion radius are the main factors to be responsible for migration energy barriers on g-Mg_3N_2. The ion radius of Li^+, Na^+, K^+, Mg^{2+}, Ca^{2+} and Al^{3+} are 0.76, 1.02, 1.38, 0.72, 1.00 and 0.54 Å, respectively. Although the radius of the Al^{3+} is the smallest of all metals, it suffered the highest barrier during the migration process. Furthermore, benefiting from unique host structure, the migration energy barriers of Na- (315 meV) and K-ion (192 meV) on g-Mg_3N_2 are even lower than Li-ion (575 meV).[48] The energy barriers for Mg-, Ca- and Al-ion migration are acceptable for a battery application considering their high capacity and low cost. What's more, both Path-1 and Path-2 can make a complete metal-ions diffusion network on the g-Mg_3N_2

surface, indicating that the charge/discharge rate of g-Mg_3N_2 is satisfactory for NLMIBs applications.

4. Summary and conclusions

In summary, we use density functional theory calculations for the first time to prove that 2D g-Mg_3N_2 can be applied as an appropriate anode material for NLMIBs. g-Mg_3N_2 possesses high theoretical storage capacity and maintain structural stability during different metal-ions intercalation process. The electronic structure of g-Mg_3N_2 becomes metallic by metal-ions intercalation. The satisfactory metal-ions migration energy barriers combined with complete 2D diffusion network ensure good rate performance of g-Mg_3N_2 as anodes. Overall, we predict theoretically that g-Mg_3N_2 has many advantages as a good anode material, such as good structural and electrochemical stability, high metal-ions storage capacities, high electronic conductivity, acceptable sequential intercalated potentials and metal-ions diffusion energy barriers, thus, it can be applied as anode material for inexpensive and promising NLMIBs.

Conflicts of interest

There are no conflicts to declare.

Acknowledgements

This work is supported by the Natural Science Foundation of China (NSFC, under Grant No. 51962010 and 11564016). The computations were partly performed on TianHe-2(A) at the National Supercomputer Center in Tianjin.

References

1 D. Larcher and J. M. Tarascon, Towards greener and more sustainable batteries for electrical energy storage, *Nat. Chem.*, 2015, **7**, 19–29.
2 J. B. Goodenough and K. S. Park, The Li-ion rechargeable battery: a perspective, *J. Am. Chem. Soc.*, 2013, **135**, 1167–1176.
3 B. Dunn, H. Kamath and J. M. Tarascon, Electrical energy storage for the grid: a battery of choices, *Science*, 2011, **334**, 928–935.
4 J. M. Tarascon and M. Armand, Issues and challenges facing rechargeable lithium batteries, *Nature*, 2001, **414**, 359–367.
5 M. A. Hannan, M. M. Hoque, A. Mohamed and A. Ayob, Review of energy storage systems for electric vehicle applications: issues and challenges, *Renewable Sustainable Energy Rev.*, 2017, **69**, 771–789.
6 Y. M. Sun, N. Liu and Y. Cui, Promises and challenges of nanomaterials for lithium-based rechargeable batteries, *Nat. Energy*, 2016, **1**, 16071.
7 N. Yabuuchi, K. Kubota, M. Dahbi and S. Komaba, Research development on sodium-ion batteries, *Chem. Rev.*, 2014, **114**, 11636–11682.
8 H. Y. Kang, Y. C. Liu, K. Z. Cao, Y. Zhao, L. F. Jiao, Y. J. Wang and H. T. Yuan, Update on anode materials for Na-ion batteries, *J. Mater. Chem. A*, 2015, **3**, 17899–17913.
9 Z. L. Jian, W. Luo and X. L. Ji, Carbon electrodes for K-ion batteries, *J. Am. Chem. Soc.*, 2015, **137**, 11566–11569.
10 H. D. Yoo, I. Shterenberg, Y. Gofer, G. Gershinsky, N. Pour and D. Aurbach, Mg rechargeable batteries: an on-going challenge, *Energy Environ. Sci.*, 2013, **6**, 2265–2279.
11 Z. J. Zhao, J. P. Yao, B. Z. Sun, S. Y. Zhong, X. L. Lei, B. Xu and C. Y. Ouyang, First-principles identification of spinel $CaCo_2O_4$ as a promising cathode material for Ca-ion batteries, *Solid State Ionics*, 2018, **326**, 145–149.
12 M. C. Lin, M. Gong, B. G. Lu, Y. P. Wu, D. Y. Wang, M. Y. Guan, M. Angell, C. X. Chen, J. Yang, B. J. Hwang and H. J. Dai, An ultrafast rechargeable aluminium-ion battery, *Nature*, 2015, **520**, 324–328.
13 Y. Xie, Y. Dall'Agnese, M. Naguib, Y. Gogotsi, M. W. Barsoum, H. L. Zhuang and P. R. C. Kent, Prediction and characterization of MXene nanosheet anodes for non-lithium-ion batteries, *ACS Nano*, 2014, **8**, 9606–9615.
14 P. Xiang, X. F. Chen, W. T. Zhang, J. F. Li, B. B. Xiao, L. S. Li and K. Deng, Metallic borophene polytypes as lightweight anode materials for non-lithium-ion batteries, *Phys. Chem. Chem. Phys.*, 2017, **19**, 24945–24954.
15 X. Y. Deng, X. F. Chen, Y. Huang, B. B. Xiao and H. Y. Du, Two-Dimensional GeP_3 as a high capacity anode material for non-lithium-ion batteries, *J. Phys. Chem. C*, 2019, **123**, 4721–4728.
16 M. J. Piernas-Munoz, E. Castillo-Martinez, O. Bondarchuk, M. Armand and T. Rojo, Higher voltage plateau cubic Prussian white for Na-ion batteries, *J. Power Sources*, 2016, **324**, 766–773.
17 X. F. Bie, K. Kubota, T. Hosaka, K. Chihara and S. Komaba, A novel K-ion battery: hexacyanoferrate(II)/graphite cell, *J. Mater. Chem. A*, 2017, **5**, 4325–4330.
18 S. W. Kim, D. H. Seo, X. H. Ma, G. Ceder and K. Kang, Electrode materials for rechargeable sodium-ion batteries: potential alternatives to current lithium-ion batteries, *Adv. Energy Mater.*, 2012, **2**, 710–721.
19 S. Okada, S. Sawa, M. Egashira, J. Yamaki, M. Tabuchi, H. Kageyama, T. Konishi and A. Yoshino, Cathode properties of phospho-olivine $LiMPO_4$ for lithium secondary batteries, *J. Power Sources*, 2001, **97–98**, 430–432.
20 X. D. Xiang, K. Zhang and J. Chen, Recent advances and prospects of cathode materials for sodium-ion batteries, *Adv. Mater.*, 2015, **27**, 5343–5364.
21 B. Xu, H. S. Lu, B. Liu, G. Liu, M. S. Wu and C. Y. Ouyang, Comparisons between adsorption and diffusion of alkali, alkaline earth metal atoms on silicene and those on silicane: insight from first-principles calculations, *Chin. Phys. B*, 2016, **25**, 067103.
22 W. Luo, F. Shen, C. Bommier, H. L. Zhu, X. L. Ji and L. B. Hu, Na-ion battery anodes: materials and electrochemistry, *Acc. Chem. Res.*, 2016, **49**, 231–240.
23 M. Kazazi, Z. A. Zafar, M. Delshad, J. Cervenka and C. X. Chen, TiO_2/CNT nanocomposite as an improved

anode material for aqueous rechargeable aluminum batteries, *Solid State Ionics*, 2018, **320**, 64–69.
24 E. Pomerantseva and Y. Gogotsi, Two-dimensional heterostructures for energy storage, *Nat. Energy*, 2017, **2**, 17089.
25 H. Zhang, Ultrathin two-dimensional nanomaterials, *ACS Nano*, 2015, **9**, 9451–9469.
26 M. R. Lukatskaya, O. Mashtalir, C. E. Ren, Y. Dall'Agnese, P. Rozier, P. L. Taberna, M. Naguib, P. Simon, M. W. Barsoum and Y. Gogotsi, Cation intercalation and high volumetric capacitance of two-dimensional titanium carbide, *Science*, 2013, **341**, 1502–1505.
27 Q. L. Sun, Y. Dai, Y. D. Ma, T. Jing, W. Wei and B. B. Huang, Ab initio prediction and characterization of Mo_2C monolayer as anodes for lithium-ion and sodium-ion batteries, *J. Phys. Chem. Lett.*, 2016, **7**, 937–943.
28 J. H. Hou, K. X. Tu and Z. F. Chen, Two-dimensional Y_2C electride: a promising anode material for Na-ion batteries, *J. Phys. Chem. C*, 2016, **120**, 18473–18478.
29 B. Mortazavi, O. Rahaman, S. Ahzi and T. Rabczuk, Flat borophene films as anode materials for Mg, Na or Li-ion batteries with ultra high capacities: a first-principles study, *Applied Materials Today*, 2017, **8**, 60–67.
30 B. Mortazavi, M. Shahrokhi, X. Y. Zhuang and T. Rabczuk, Boron-graphdiyne: a superstretchable semiconductor with low thermal conductivity and ultrahigh capacity for Li, Na and Ca ion storage dagger, *J. Mater. Chem. A*, 2018, **6**, 11022–11036.
31 S. F. Lei, X. F. Chen, B. B. Xiao, W. T. Zhang and J. Liu, Excellent electrolyte wettability and high energy density of B_2S as a two-dimensional Dirac anode for non-lithium-ion batteries, *ACS Appl. Mater. Interfaces*, 2019, **11**, 28830–28840.
32 I. Demiroglu, F. M. Peeters, O. Gulseren, D. Cakir and C. Sevik, Alkali metal intercalation in MXene/graphene heterostructures: a new platform for ion battery applications, *J. Phys. Chem. Lett.*, 2019, **10**, 727–734.
33 P. F. Liu, L. J. Zhou and L. M. Wu, A graphene-like Mg_3N_2 monolayer: high stability, desirable direct band gap and promising carrier mobility, *Phys. Chem. Chem. Phys.*, 2016, **18**, 30379–30384.
34 C. Y. Ouyang and L. Q. Chen, Physics towards next generation Li secondary batteries materials: a short review from computational materials design perspective, *Sci. China: Phys., Mech. Astron.*, 2013, **56**, 2278–2292.
35 L. M. Zheng, Z. Q. Wang, M. S. Wu, B. Xu and C. Y. Ouyang, Jahn-Teller type small polaron assisted Na diffusion in $NaMnO_2$ as a cathode material for Na-ion batteries, *J. Mater. Chem. A*, 2019, **7**, 6053–6061.
36 H. W. Wang, M. S. Wu, X. L. Lei, Z. F. Tian, B. Xu, K. Huang and C. Y. Ouyang, Siligraphene as a promising anode material for lithium-ion batteries predicted from first-principles calculations, *Nano Energy*, 2018, **49**, 67–76.
37 G. Kresse and J. Furthmüller, Efficient iterative schemes for ab initio total-energy calculations using a plane-wave basis set, *Phys. Rev. B: Condens. Matter Mater. Phys.*, 1996, **54**, 11169–11186.
38 P. E. Blöchl, Projector augmented-wave method, *Phys. Rev. B: Condens. Matter Mater. Phys.*, 1994, **50**, 17953–17979.
39 G. Kresse and J. Joubert, From ultrasoft pseudopotentials to the projector augmented-wave method, *Phys. Rev. B: Condens. Matter Mater. Phys.*, 1999, **59**, 1758–1775.
40 T. Bucko, J. Hafner, S. Lebegue and J. G. Angyan, Improved description of the structure of molecular and layered crystals: ab initio DFT calculations with van der Waals corrections, *J. Phys. Chem. A*, 2010, **114**, 11814–11824.
41 S. Grimme, Semiempirical GGA-type density functional constructed with a long-range dispersion correction, *J. Comput. Chem.*, 2006, **27**, 1787–1799.
42 H. J. Monkhorst and J. D. Pack, Special points for Brillouin-zone integrations, *Phys. Rev. B: Solid State*, 1976, **13**, 5188–5192.
43 G. Henkelman and H. Jónsson, Improved tangent estimate in the nudged elastic band method for finding minimum energy paths and saddle points, *J. Chem. Phys.*, 2000, **113**, 9901–9904.
44 G. Henkelman, A. Arnaldsson and H. Jónsson, A fast and robust algorithm for Bader decomposition of charge density, *Comput. Mater. Sci.*, 2006, **36**, 354–360.
45 A. Togo and I. Tanaka, First principles phonon calculations in materials science, *Scr. Mater.*, 2015, **108**, 1–5.
46 F. Zhou, M. Cococcioni, C. A. Marianetti, D. Morgan and G. Ceder, First-principles prediction of redox potentials in transition-metal compounds with LDA + U, *Phys. Rev. B: Condens. Matter Mater. Phys.*, 2004, **70**, 235121.
47 X. M. Zhang, J. P. Hu, Y. C. Cheng, H. Y. Yang, Y. G. Yao and S. Y. A. Yang, Borophene as an extremely high capacity electrode material for Li-ion and Na-ion batteries, *Nanoscale*, 2016, **8**, 15340–15347.
48 L. X. Xiong, J. P. Hu, S. C. Yu, M. S. Wu, B. Xu and C. Y. Ouyang, Density functional theory prediction of Mg_3N_2 as a high-performance anode material for Li-ion batteries, *Phys. Chem. Chem. Phys.*, 2019, **21**, 7053–7060.
49 W. W. Luo, H. W. Wang, J. P. Hu, S. Q. Liu and C. Y. Ouyang, Curvature induced improvement of Li/Na storage in Ca_2N nanotubes, *Appl. Surf. Sci.*, 2018, **459**, 406–410.
50 J. P. Hu, C. Y. Ouyang, S. Y. A. Yang and H. Y. Yang, Germagraphene as a promising anode material for lithium-ion batteries predicted from first-principles calculations, *Nanoscale Horiz.*, 2019, **4**, 457–463.